Pergamon

Int. J. Heat Mass Transfer. Vol. 39, No. 9, pp. 1785–1795, 1996

0017-9310/96 $15.00+0.00

0017-9300(95)00292-1

Numerical simulation of heat penetration through a vertical rectangular phase change material/air composite cell

C. J. HO and C. H. CHU

Department of Mechanical Engineering, National Cheng Kung University, Tainan, Taiwan 70101, Republic of China

(*Received* 27 *March* 1995 *and in final form* 24 *July* 1995)

Abstract—In this paper a numerical simulation of transient heat penetration through a vertical rectangular composite cell, filled with a solid–liquid phase change material (PCM) and air layer, is presented. Inside the composite cell the PCM layer is separated from the air layer by a solid partition of finite thickness. The buoyancy-induced flows developed in both the air-filled layer and the molten PCM zone inside the PCM layer were modeled as two-dimensional laminar Newtonian fluid flow adhering to the Boussinesq approximation. Meanwhile, two-dimensional conduction heat transfer accounted for the unmelted solid PCM region as well as the solid partition. The numerical results for the composite cell with a thin diathermal partition demonstrate that by means of the latent-heat absorption inside the PCM layer, heat penetration across the composite cell can be greatly retarded over an effective duration until a critical instant, around which the melting front of the PCM reaches the partition wall. Such an effective thermal protection duration is found to be a strong function of the modified Rayleigh number, the modified Stefan number, the subcooling factor, the relative PCM thickness ratio, and the aspect ratio of the composite cell. A geometry of a shallow rectangular composite cell having a larger PCM/air thickness ratio is found to be preferable for effective thermal protection applications. In addition, the effect of a solid partition of finite thickness and conductivity on thermal protection efficacy of the PCM/air composite cell is examined.

INTRODUCTION

This article presents a numerical investigation aiming to elucidate the thermal protection performance of a vertical PCM/air composite cellular structure modeled as a rectangular composite cell, depicted schematically in Fig. 1. The composite cell is filled with PCM and air layers separated by a solid partition of finite thickness. Effective thermal insulation or thermal protection is of crucial importance in numerous industrial processes and energy conservation in buildings. One of the passive thermal protection techniques receiving great interest is the phase change thermal control utilizing solid–liquid phase change material (PCM) due to its inherent advantage of simplicity and reliability. Typically, latent-heat absorption phenomenon associated with melting of a suitable PCM can be effectively incorporated to delay or mitigate heat penetration through bounding surfaces of the system, in turn accomplishing the objective of thermal protection or thermal control. In the literature, various geometric configurations have been considered for the phase-change thermal control applications. Bain *et al.* [1] analyzed melting heat transfer in a PCM-filled rectangular cavity for spacecraft thermal control. The finned rectangular PCM-filled cavity was further considered for thermal control of electronic equipment [2, 3]. Recently, Cao and Faghri [4] numerically simulated transient heat penetration characteristics through a PCM-filled wall as a thermal protection device from a localized intense laser beam.

In this study, to delineate thermal protection performance of the PCM/air composite cell under consideration, numerical simulations via a finite difference method have been undertaken for the resulting transient conjugate heat penetration process. Results obtained are presented for the time-dependent variations of temperature field and heat penetration rate as functions of the pertinent parameters of the problem considered.

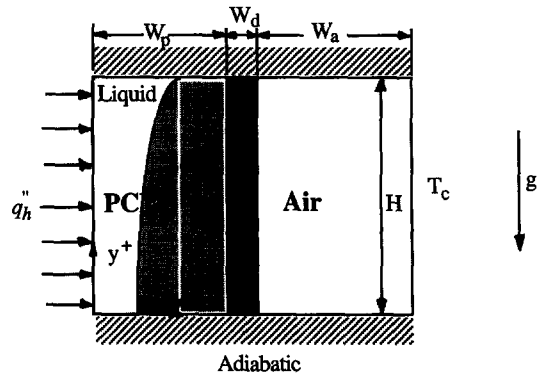

Fig. 1. Schematic diagram of physical configuration of a PCM/air composite cell.

NOMENCLATURE

A	aspect ratio of composite cell $(W_p+W_d+W_a)/H$
A_a	dimensionless thickness of air layer, W_a/H
A_d	dimensionless thickness of solid partition, W_d/H
A_p	dimensionless thickness of PCM layer, W_p/H
c_p	specific heat
Fo	Fourier number, $\alpha_l t/H^2$
g	gravitational acceleration
H	height of enclosure
k	thermal conductivity
L	latent heat
Nu	Nusselt number
Pr	Prandtl number, ν_l/α_l
q''	heat flux
Q	dimensionless heat flux
$\bar{Q}_{r,i}$	instantaneous, fractional averaged heat flux, equation (13)
$\bar{Q}_{r,t}$	total, fractional averaged heat flux, equation (14)
Ra^*	modified Rayleigh number, $g\beta q''_h H^4/(k_l \nu_l \alpha_l)$
S	dimensionless position of solid–liquid interface
Sc^*	subcooling factor, $(T_f-T_c)k_l/(q''_h H)$
Ste^*	modified Stefan number, $c_{p,l}q''_h H/(Lk_l)$
t	time
T	temperature
V_m	volume of liquid PCM
V_o	total volume of PCM layer
V^*	volumetric fraction of liquid PCM, V_m/V_o
W	width of composite cell, $W_p+W_d+W_a$
W_a	width of air layer
W_d	width of solid partition
W_p	width of PCM layer
x^+, y^+	Cartesian coordinates
x, y	dimensionless coordinates, x^+/H, y^+/H.

Greek symbols

α	thermal diffusivity, $k/(\rho c_p)$
β	thermal volumetric expansion coefficient
θ	dimensionless temperature, $(T-T_f)k_l/(q''_h H)$
ν	kinematic viscosity
ρ	density
ψ^+	stream function
ψ	dimensionless stream function, ψ^+/α_l
ω^+	vorticity
ω	dimensionless vorticity, $\omega^+ H^2/\alpha_l$.

Subscripts

a	air
c	cold surface
cr	critical value
d	dividing partition
f	fusion point
h	hot surface
i	instantaneous quantity
l	liquid phase of PCM
r	fractional quantity
s	solid phase of PCM
t	time-averaged quantity.

Superscripts

*	ratio of a quantity to that of liquid PCM
-	surface-averaged value.

ANALYSIS

Model equations

For the model geometry considered in the present work shown in Fig. 1, the vertical rectangular composite cell of dimensions $W \times H$ is initially at a uniform temperature of T_c ($< T_f$) so that the solid PCM layer is subcooled. At a certain instant $t = 0$, incoming heat is received from the left vertical wall inasmuch that it is uniformly heated with a constant heat flux q''_h, while the right vertical wall of the cell remains isothermal at T_c. The horizontal endwalls of the composite cell are assumed adiabatic. Moreover, the solid partition of thickness W_d, separating the PCM and air layers, is located at W_p. The ensuing transient conjugate heat transfer process inside the composite cell is modeled to be two-dimensional with the following assumptions:

(1) Buoyancy-induced convection in the liquid PCM region and the air-filled subcell is laminar Newtonian fluid flow adhering to the Boussinesq approximation.

(2) Thermophysical properties of the PCM and air layers are independent of temperature.

(3) The viscous dissipation in the fluid flow and volume change of PCM associated with solid–liquid phase change are negligible.

(4) Radiation effect in the air-filled subcell is neglected.

With the foregoing assumptions, the dimensionless governing differential equations for buoyancy-driven heat and fluid flow fields, developed in both the melt

region inside the PCM layer and the air-filled subcell, can be, respectively, expressed in terms of the vorticity ω, the stream function ψ and the temperature θ as follows.

In the melt region of PCM layer

$$\frac{\partial\omega}{\partial Fo}+\frac{\partial\psi}{\partial y}\frac{\partial\omega}{\partial x}-\frac{\partial\psi}{\partial x}\frac{\partial\omega}{\partial y}=Pr\left(\frac{\partial^2\omega}{\partial x^2}+\frac{\partial^2\omega}{\partial y^2}\right)+PrRa^*\frac{\partial\theta}{\partial x} \quad (1)$$

$$\frac{\partial^2\psi}{\partial x^2}+\frac{\partial^2\psi}{\partial y^2}=-\omega \quad (2)$$

$$\frac{\partial\theta}{\partial Fo}+\frac{\partial\psi}{\partial y}\frac{\partial\theta}{\partial x}-\frac{\partial\psi}{\partial x}\frac{\partial\theta}{\partial y}=\left(\frac{\partial^2\theta}{\partial x^2}+\frac{\partial^2\theta}{\partial y^2}\right); \quad (3)$$

in the air-filled subcell

$$\frac{\partial\omega}{\partial Fo}+\frac{\partial\psi}{\partial y}\frac{\partial\omega}{\partial x}-\frac{\partial\psi}{\partial x}\frac{\partial\omega}{\partial y}=\nu_a^*Pr\left(\frac{\partial^2\omega}{\partial x^2}+\frac{\partial^2\omega}{\partial y^2}\right)+\beta_a^*PrRa^*\frac{\partial\theta}{\partial x}. \quad (4)$$

$$\frac{\partial^2\psi}{\partial x^2}+\frac{\partial^2\psi}{\partial y^2}=-\omega \quad (5)$$

$$\frac{\partial\theta}{\partial Fo}+\frac{\partial\psi}{\partial y}\frac{\partial\theta}{\partial x}-\frac{\partial\psi}{\partial x}\frac{\partial\theta}{\partial y}=\alpha_a^*\left(\frac{\partial^2\theta}{\partial x^2}+\frac{\partial^2\theta}{\partial y^2}\right). \quad (6)$$

Moreover, two-dimensional conduction is accounted for in the unmelted region of the PCM layer, as well as for the solid partition, with the following governing equations:

In the unmelted PCM region

$$\frac{\partial\theta}{\partial Fo}=\alpha_s^*\left(\frac{\partial^2\theta}{\partial x^2}+\frac{\partial^2\theta}{\partial y^2}\right) \quad (7)$$

and for the solid partition

$$\frac{\partial\theta}{\partial Fo}=\alpha_d^*\left(\frac{\partial^2\theta}{\partial x^2}+\frac{\partial^2\theta}{\partial y^2}\right). \quad (8)$$

The dimensionless initial and boundary conditions for the problem are:

$$Fo=0;\quad \omega=\psi=0,\theta=-Sc^* \quad (9)$$

$Fo>0$;

$$x=0,\quad 0\leqslant y\leqslant 1;\quad \psi=\frac{\partial\psi}{\partial y}=0,$$

$$\frac{\partial\theta}{\partial x}=-1 \text{ (liquid PCM)}$$

or

$$-\frac{1}{k_s^*}\text{(solid PCM)} \quad (10a)$$

$$x=A,\quad 0\leqslant y\leqslant 1;\quad \psi=\frac{\partial\psi}{\partial x}=0,\quad \theta=-Sc^* \quad (10b)$$

$$y=0,\quad \text{or}\quad 1,0\leqslant x\leqslant A;\quad \psi=\frac{\partial\psi}{\partial x}=0,\quad \frac{\partial\theta}{\partial y}=0. \quad (10c)$$

Note that the iso-flux condition in equation (10a) depends on the phase (liquid or solid) of PCM in contact with the iso-flux-heated wall. At the solid–liquid interface in the PCM layer, we have

$$\theta=0,\quad \text{and}\quad \left[1+\left(\frac{\partial S}{\partial y}\right)^2\right]\left(k_s^*\frac{\partial\theta}{\partial x}\bigg|_s-\frac{\partial\theta}{\partial x}\bigg|_l\right)=\frac{\rho_s^*}{Ste^*}\frac{\partial S}{\partial Fo}. \quad (11)$$

The dimensionless local heat penetration rate onto the isothermally cold wall of composite cell is expressed as

$$Q_c=-\frac{\partial\theta}{\partial x}\bigg|_{x=A}=\frac{q_c''}{k_a^*q_h''}, \quad (12)$$

which in effect denotes the local fractional heat penetration flux through the composite cell. Moreover, the quantities of practical interest to thermal protection applications are the instantaneous and time-averaged, fractional surface-averaged heat penetrations across the composite cell onto the cold wall, which are, respectively, defined as

$$\bar{Q}_{r,i}=k_a^*\int_0^1 Q_c\,dy=\frac{\bar{q}_c''}{q_h''} \quad (13)$$

and

$$\bar{Q}_{r,t}=\frac{1}{Fo}\int_0^{Fo}\bar{Q}_{r,i}\,dFo=\frac{\int_0^t\bar{q}_c''\,dt}{q_h''t}. \quad (14)$$

Method of solution

The foregoing system of the model equations, equations (1)–(9), for the present problem has been solved subjected to the boundary conditions, equations (10) and (11), using a finite difference method. The finite difference discretization involves the second-order central difference scheme for the spatial derivatives, except for the convective terms, which are treated with the second upwind difference scheme. The temporal derivatives are approximated by the first-order backward difference formula. Moreover, the moving solid–liquid boundary arising in the PCM layer is treated by a solution algorithm devised in earlier work [5], in which the energy balance equation, equation (11), is used to calculate explicitly the solid–liquid interface position.

A uniform mesh system having grid sizes of

$\Delta x = 0.02$ and $\Delta y = 0.025$ in the horizontal and vertical direction, respectively, was adopted for the present simulation based on a series of grid-convergence test. For instance, using different uniform mesh systems of 41 (x-direction) $\times$ 31(y-direction), 51×41, 77×51 for $Ra^* = 10^6$, $Ste^* = 0.1$, $Sc^* = 0.5$, $A_d = 0.2$, $A_p = A_a = 0.4$ resulted in a maximum difference of less than 2% in the transient values of stream function extreme and heat transfer rates. A time step of 0.01 was found to be sufficiently small for the present simulation.

RESULTS AND DISCUSSION

In the present study, n-octadecane ($Pr = 46.2$) was selected as the PCM filled in the composite cell and the resulting values of relevant thermophysical property ratios have been taken as: $k_s^* = 2.41$, $k_a^* = 0.177$, $\alpha_s^* = 2.588$, $\alpha_a^* = 245.7$, $\beta_a^* = 4.163$, $\nu_a^* = 3.12$, and $\rho_s^* = 1.037$. Numerical simulations have been undertaken to unveil effects of the geometrical and physical parameters on transient heat penetration through the PCM/air composite cell in the following ranges: $A = 0.5 \sim 2.0$; $A_p/A_a = 0.333 \sim 3.0$; $A_d = 0 \sim 0.2$; $Ste^* = 0.05 \sim 0.4$; $Sc^* = 0.25 \sim 1.0$; and $Ra^* = 10^4 \sim 5 \times 10^6$. First, the results for the PCM/air layers divided by a thin diathermal partition ($A_d = 0$) will be presented in detail in terms of volumetric melting rate of PCM layer, V^*; fractional heat penetration rates, $\bar{Q}_{r,i}$ and $\bar{Q}_{r,t}$; and temperature of the isoflux-heated wall, θ_h. Then the effects of a partition with finite thickness and conductivity on heat penetration across the composite cell will be examined.

PCM/air layers divided by a thin diathermal partition ($A_d = 0$)

Typical evolution of the temperature distribution and flow field developed inside an isoflux-heated unit-aspect-ratio composite cell is presented in Fig. 2 by means of a sequence of contour plots of isotherms (left) and streamlines (right) for $Ste^* = 0.1$, $Sc^* = 0.5$, $Ra^* = 10^6$, and $A_p/A_a = 1$. The solid–liquid interface contour in the plots is denoted by a dashed line. At the early stage of the heat penetration process, as exemplified in Fig. 2a for $Fo = 1.0$, the isotherm distribution over the entire composite cell reveals a conduction-dominated heat transfer regime. As can be expected, the buoyancy-induced convective flows in both the liquid PCM and air regions strengthen gradually with time, as indicated by the growing magnitude of the stream function extreme shown in Fig. 2. It should be noticed here that due to its higher thermal diffusivity and thermal expansion coefficient, the magnitude of the dimensionless steam-function extreme in the air region appears to be much larger than that of the liquid PCM region. At $Fo = 2.0$, Fig. 2b, a natural-convection dominated melting pattern is already established in the PCM layer; the top portion of the melt region is seen to expand much faster due to more melting taking place there. As the melting process further proceeds, the top portion of the solid PCM layer is melted through, such that the melting front reaches the diathermal partition, providing a direct heat penetrating path between the liquid PCM and air regions. Accordingly, heat flux across the top portion of the partition wall is greatly enhanced. Meanwhile, the melting front begins to propagate downward along the partition wall as a result of build-up of the vertical temperature gradient in that region, as illustrated in Fig. 2c for $Fo = 5.0$. The unmelted PCM can be readily seen shrinking downward to the bottom right corner of the PCM subcell; and the vortex centers of clockwise recirculating flow structures in the air layer and the molten PCM zone tend to shift upward and downward, respectively, due to the increasing heat penetration through the top portion of the partition. In Fig. 2d, the steady-state temperature and flow fields in the composite cell are shown. The solid PCM layer has been completely melted and a relatively minute temperature gradient prevails in the molten PCM layer.

Temporal variations of the volumetric melting rate V^*, the instantaneous and time-averaged, fractional heat penetration across the composite cell, $\bar{Q}_{r,i}$ and $\bar{Q}_{r,t}$, are illustrated in Fig. 3 for different values of the modified Stefan number Ste^* with $Ra^* = 10^6$, $Sc^* = 0.5$, and $A_p = A_a = 0.5$. From Fig. 3a it can be seen that the increase of Ste^* accelerates greatly the melting process of the PCM layer. To the thermal protection application, the instantaneous fractional heat flux across the composite cell onto the cold wall, $\bar{Q}_{r,i}$, is of practical interest. It is evident from an overview of Fig. 3b that the temporal trend of $\bar{Q}_{r,i}$ exhibits a ramp-like increase from a quasi-steady plateau, then approaching gradually the steady-state value of unity. At $Ste^* = 0.05$, for instance, over an initial heating period, $\bar{Q}_{r,i}$ displays a rapid increase up to a quasi-steady value of about 0.16, which amounts to only less than 16% of the incident heat flux at the hot wall, has penetrated across the PCM/air composite layer reaching the isothermal cold wall. Until a certain instant of time $Fo_{cr} \approx 6.8$ about which the melting front reaches the partition, the quasi-steady variation of $\bar{Q}_{r,i}$ gives way to the ramp-like rise. The time interval from the beginning of the heating process down to Fo_{cr} can be viewed as an effective thermal-protection period of the PCM/air composite cell. Increase of Ste^* tends to advance the onset of the ramp-like uprising of $\bar{Q}_{r,i}$, resulting in a shorter effective thermal protection period Fo_{cr}, due to the accelerated melting rate in the PCM layer. For the time-averaged fractional heat penetration $\bar{Q}_{r,t}$, as presented in Fig. 3c, a two-stage temporal variation prevails. After an initial period of slow increase with time, curves of the time-averaged fractional heat penetration $\bar{Q}_{r,t}$ evolve drastically into a nearly linear time dependence with a markedly higher constant gradient, another indication of reaching steady-state heat penetration across the composite cell. A higher Ste^* tends to further promote the above-

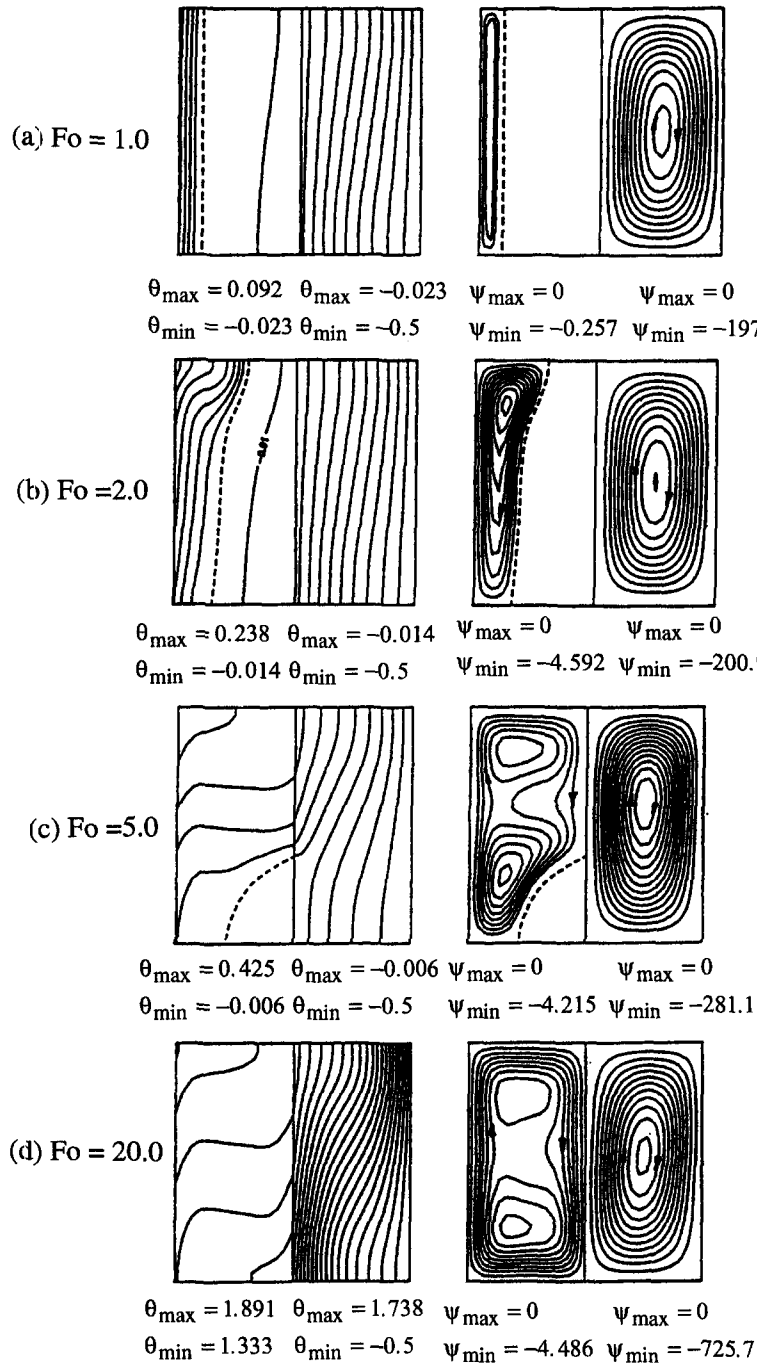

Fig. 2. Typical evolution of isotherms (left) and streamlines (right) in the composite PCM/air cell with $Ra^* = 10^6$, $Ste^* = 0.1$, $Sc^* = 0.5$, $A = 1$, and $A_p = A_a$.

described temporal variation of $\bar{Q}_{r,t}$. Another interesting message that can be inferred from Fig. 3c is that as the heating process approaches the steady state, the values of $\bar{Q}_{r,t}$ still remains to be far less than unity, reflecting only small fraction of the time-averaged heat input at the isoflux-heated wall is allowed to penetrate through the composite cell. Moreover, the effect of Ste^* is conveyed in Fig. 4 on the temperature history on the isoflux-heated wall of the composite cell. It can be readily noticed that the resemblance to that observed for the instantaneous fractional heat penetration $\bar{Q}_{r,i}$ shown in Fig. 3b, the variation of the surface-averaged temperature $\bar{\theta}_h$, or the maximum temperature, $\theta_{h,max}$, of the isoflux-heated wall features a ramp-like increase with time for $Fo \geqslant Fo_{cr}$. It may be further observed that the steady-state values of $\bar{\theta}_h$ and $\theta_{h,max}$ appear to be independent of Ste^*, owing to completion of the melting process in the PCM layer.

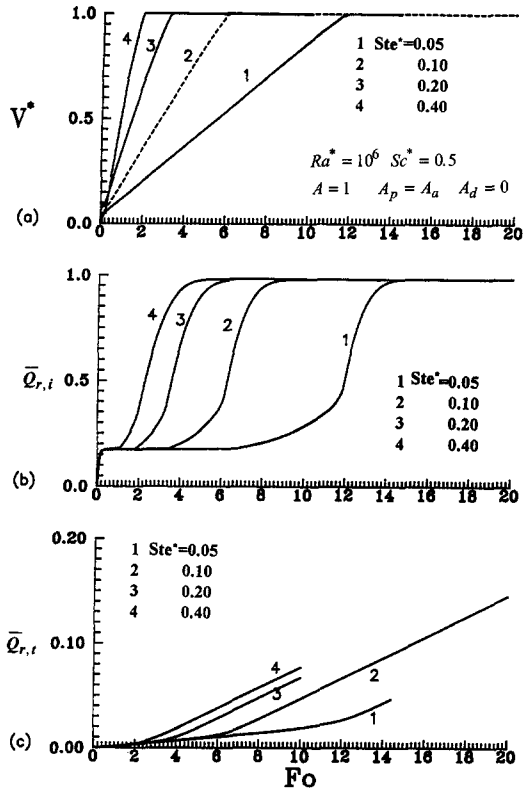

Fig. 3. Histories of (a) melting rate, (b) instantaneous, and (c) time-averaged, fractional heat penetration onto the cold wall of the composite cell with various Ste^* at $Ra^* = 10^6$, $Sc^* = 0.5$, $A = 1$, and $A_p = A_a$.

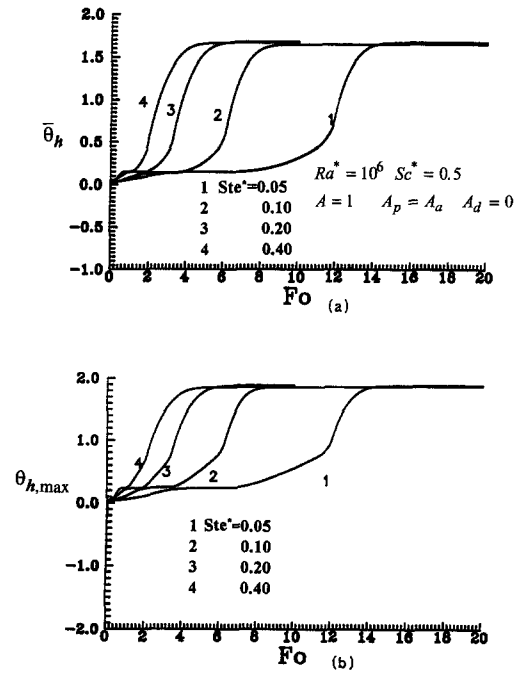

Fig. 4. Dependence of (a) surface-averaged and (b) the maximum temperature at the isoflux-heated wall of the composite cell on Ste^*.

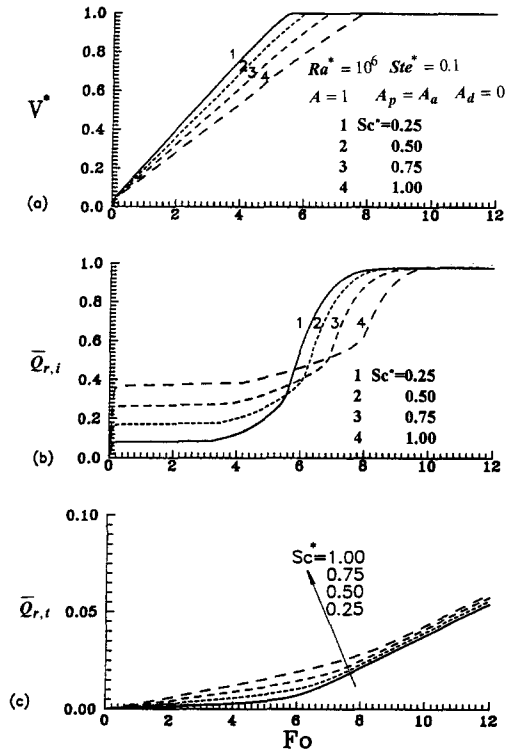

Fig. 5. Influence of Sc^* on evolution of (a) melting rate, (b) instantaneous, and (c) time-averaged, fractional heat penetration onto the cold wall of the composite cell at $Ra^* = 10^6$, $Ste^* = 0.1$, $A = 1$, and $A_p = A_a$.

Next the influence of subcooling factor Sc^* is exemplified in Figs. 5 and 6. As expected, a higher subcooling factor causes a slower melting rate in the PCM layer, as indicated by the curves of V^* in Fig. 5a. As for the effective thermal protection period Fo_{cr} revealed in the temporal curves of $\bar{Q}_{r,i}$ in Fig. 5b, one can observe that the decelerated melting rate of PCM, due to the increase of Sc^*, gives rise to delaying the onset of the ramp-like rise of $\bar{Q}_{r,i}$ and thus, a longer effective thermal protection period. On the other hand, the subcooling exerts a substantial bearing on the quasi-steady values of $\bar{Q}_{r,t}$ prior to its ramp-like uprising; a higher Sc^* induces a markedly higher quasi-steady instantaneous fractional heat penetration onto cold wall. This is largely due to the enhanced extraction of sensible heat through the unmelted PCM region and the air layer associated with the increase of Sc^*. Furthermore, the fanning out of the curves of Fig. 5c from the beginning of the heating process gives an immediate indication of the effect of subcooling on the time-averaged fractional heat penetration $\bar{Q}_{r,t}$. The increase of Sc^* in general results in the increase of time-averaged heat penetration across the composite cell. As a result of the increase of $\bar{Q}_{r,t}$ due to subcooling, the surface-averaged or maximum temperature of the isoflux-heated wall attains a substantially lower steady-state value, but at a later time as the subcooling factor is increased, as depicted in Fig. 6.

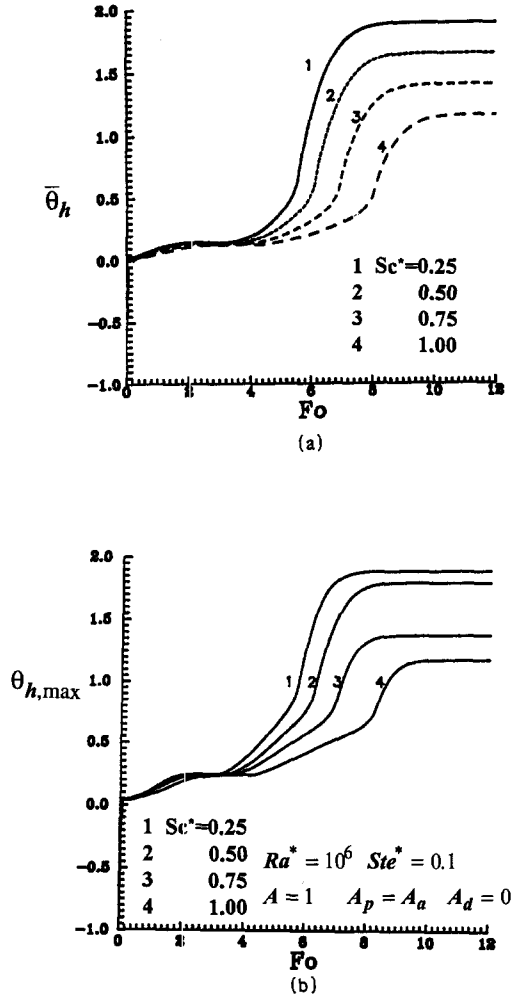

Fig. 6. Effect of Sc^* on (a) surface-averaged and (b) the maximum temperature at the isoflux-heated wall of the composite cell.

In order to relate effect of the modified Rayleigh number explicitly to the heat flux incident onto the composite cell q''_h, parametric calculations have been carried out for various Ra^* while keeping the product of Ste^* and Sc^* (since the heat flux q''_h also appears in both the parameters Ste^* and Sc^*) and other geometric parameters fixed. It should be noted that the product of Ste^* and Sc^* $(=c_{p,l}(T_f - T_c)/L)$ essentially denotes the ratio of the sensible heat capacity in the subcooled solid PCM with respect to the latent heat of fusion. As can be expected, with the increase of heat flux input by the increase of Ra^*, the melting process in the PCM layer is greatly accelerated so that V^* displays a stiffer increasing rate with a higher Ra^*, as demonstrated in Fig. 7a. Further, from Fig. 7b, c, the effects of increase of Ra^* on the instantaneous and time-averaged heat penetration rates appear to be rather the opposite to those found for the increase of the subcooling shown in Fig. 5. A higher Ra^* leads to a much shorter effective protection period, but a substantially lower quasi-steady value of $\bar{Q}_{r,i}$ for $Fo \geqslant Fo_{cr}$. In addition, the time-averaged fractional heat penetration across the composite cell exhibits a marked dependence on the modified Rayleigh number.

Now, we will turn our attention to the effects of the geometric parameters, such as the aspect ratio of the composite PCM/air layer A and the thickness ratio of the PCM layer to the air layer A_p/A_a. In Fig. 8, the relations of the melting rate and fractional heat penetration reaching the cold wall with the aspect ratio of the composite layer A are conveyed for $Ste^* = 0.1$, $Sc^* = 0.5$, $Ra^* = 10^6$, and $A_p/A_a = 1$. Completion of the PCM melting process, and thereby establishment of a steady-state heat transfer across the composite layer are, as expected, greatly delayed with the increase of aspect ratio A. This is largely attributed to the increase of PCM thickness, and thus the latent-heat-absorption capacity with the increase of A. Accordingly, the increase of the aspect ratio of the composite layer leads to a prolonged effective thermal-protection duration Fo_{cr} as displayed in Fig. 8b. Moreover, the increase of A has a bearing on the time-averaged fractional heat flux onto the cold wall so that a marked reduction of $\bar{Q}_{r,t}$ is detected in Fig. 8c. In Fig. 9 the deviations among curves of the surface-averaged or the maximum temperature of the isoflux-heated wall clearly illustrate the influence of the aspect ratio A; a shallow PCM/air composite cell ($A > 1$) tends to delay substantially the establishment of the

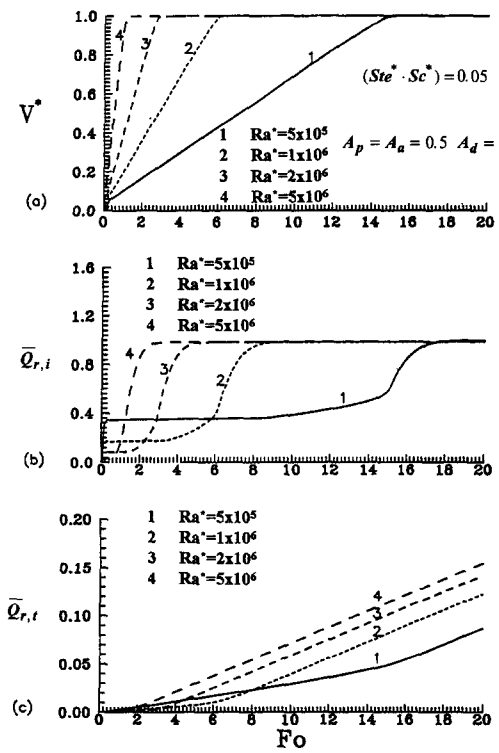

Fig. 7. Dependence of timewise variation of (a) melting rate, (b) instantaneous, and (c) time-averaged, fractional heat penetration onto the cold wall of the composite cell on Ra^* with $(Ste^*Sc^*) = 0.05$, $A = 1$, and $A_p = A_a$.

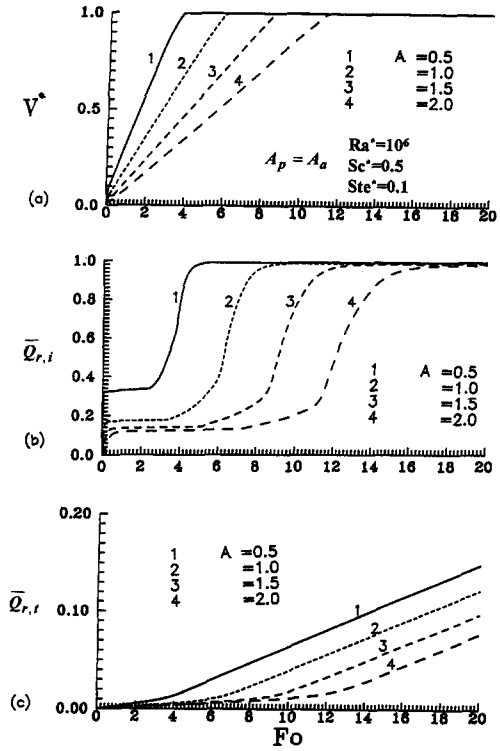

Fig. 8. Temporal variations of (a) melting rate, (b) instantaneous, and (c) time-averaged, fractional heat penetration onto the cold wall of the composite cell at various A with $Ste^* = 0.1$, $Sc^* = 0.5$, $Ra^* = 10^6$, and $A_p = A_a$.

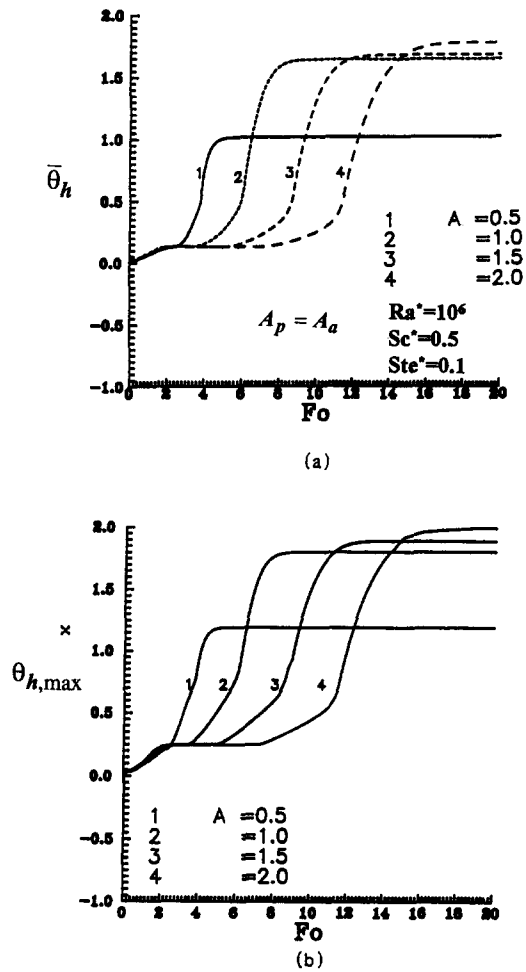

Fig. 9. Histories of (a) the surface-averaged and (b) the maximum temperature at the isoflux-heated wall at various A.

steady-state heat transfer regime, but at a higher steady-state value of $\bar{\theta}_h$ or $\theta_{h,max}$.

Next, the influence of the relative PCM/air thickness ratio is examined by varying A_p/A_a while keeping the aspect ratio of the entire composite layer A fixed at unity, as delineated in Fig. 10 for $Ste^* = 0.1$, $Sc^* = 0.5$, and $Ra^* = 10^6$. Reducing the relative thickness ratio A_p/A_a with a fixed A in effect gives a relatively thinner PCM layer, and the resulting accelerated melting behavior as shown in Fig. 10a can be readily expected. It should be noted that the time span required for completion of the melting process per unit PCM thickness (not shown here) is found to increase markedly with the increase of A_p/A_a. Moreover, an increase of A_p/A_a entails an increase of latent-heat-absorption capacity of the composite cell, and thereby induces not only a prolonged effective thermal protection duration Fo_{cr}, as shown in Fig. 10b, but also a smaller time-averaged fractional heat penetration across the composite cell as depicted in Fig. 10c. Accordingly, a marked reduction of the averaged or maximum temperature at the isoflux-heated wall with an increase of A_p/A_a can be expected, as demonstrated in Fig. 11.

The foregoing-elaborated parametric effects can be further manifested from correlation of the results of steady-state averaged Nusselt number at the isoflux-heated wall $\overline{Nu}_h$, as well as of the effective thermal protection duration Fo_{cr} with the pertinent parameters, which have been, respectively, developed using a least-square regression analysis for $Ra^* = 5\times10^5 - 5\times10^6$, $Ste^* = 0.05$–0.4, $Sc^* = 0.25$–2.0, $A = 0.5$–2.0, $A_p/A_a = 1$ and $A_d = 0$ as follows:

$$\overline{Nu}_h = 1/\bar{\theta}_h = 0.0087(Ra^*)^{0.331}(Sc^*)^{0.315}(A)^{-0.392} \tag{15}$$

with an average deviation of 4.99% and a correlation coefficient of 0.991, and

$$Fo_{cr} = 2.81(Ra^*)^{-0.119}(Ste^*)^{-0.889}(Sc^*)^{0.174}(A)^{0.746} \tag{16}$$

with an average deviation of 4.22% and a correlation coefficient of 0.994.

PCM/air layer divided by a partition with finite thickness

The effect of a partition of finite thickness and thermal conductivity on heat penetration behavior through the PCM/air composite cell will now be presented by considering acrylic [$k = 0.19$ W (m·K)$^{-1}$]

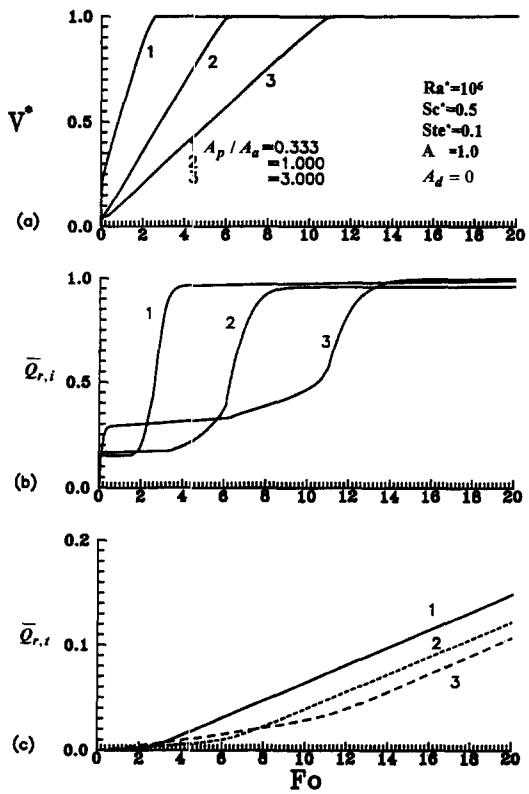

Fig. 10. Effect of relative thickness ratio on temporal profiles of (a) melting rate, (b) instantaneous, and (c) time-averaged, fractional heat penetration onto the cold wall of the composite cell at $Ra^* = 10^6$, $Ste^* = 0.1$, and $A = 1$.

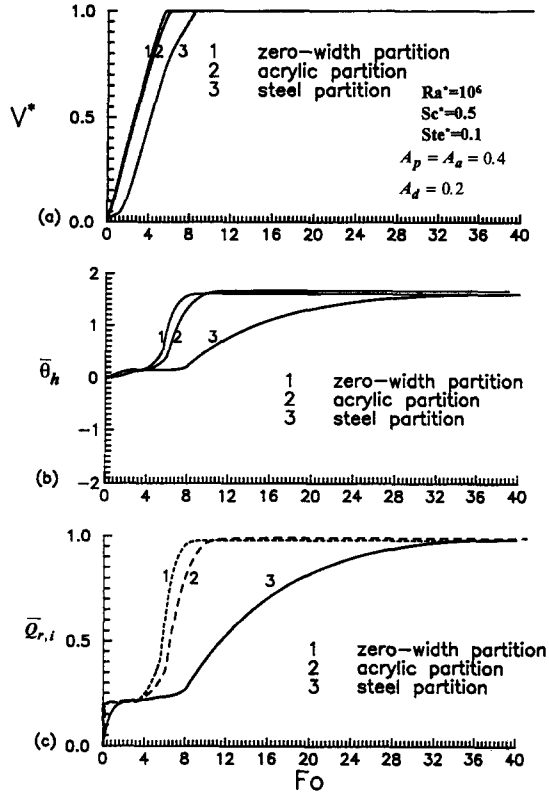

Fig. 12. Temporal variations of (a) the melting rate, (b) the surface-averaged hot wall temperature, and (c) the instantaneous fractional heat penetration through a composite cell divided with a partition of finite thickness and conductivity.

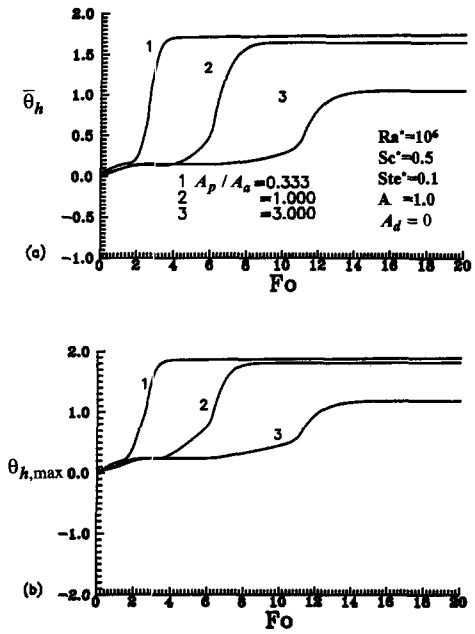

Fig. 11. Histories of (a) the surface-averaged and (b) the maximum temperature at the isoflux-heated wall with various A_p/A_a.

or stainless steel [$k = 14.3$ W (m·K)$^{-1}$] as the partition material. In Fig. 12 the histories of the melting rate of the PCM layer, the averaged temperature of the isoflux-heated wall, and the instantaneous fractional heat penetration through a unit-aspect-ratio PCM/air composite cell divided by an acrylic or stainless steel partition of thickness $A_d = 0.2$ are exemplified for $Sc^* = 0.5$, $Ste^* = 0.1$, $Ra^* = 10^6$, and $A_p = A_a$. For comparison, results for the thin diathermal partition ($A_d = 0$) are also included in Fig. 12. As shown in Fig. 12a, the approximately linear melting rate in the composite cell with steel partition exhibits a marked reduction in comparison with that of diathermal partition; while only a minutely lower melting rate is detected with the acrylic partition. This can be attributed to the fact, as will be shown later, that the steel partition due to its high conductivity remains essentially isothermal, and hence, acts as a thermal barrier to heat penetration from the PCM layer into the air-filled subcell. As a result of the markedly decelerated melting process in the PCM layer with the steel partition, the averaged temperature of the isoflux-heated wall or the instantaneous fractional heat penetration through the composite cell approaches their steady-state value in a much slower

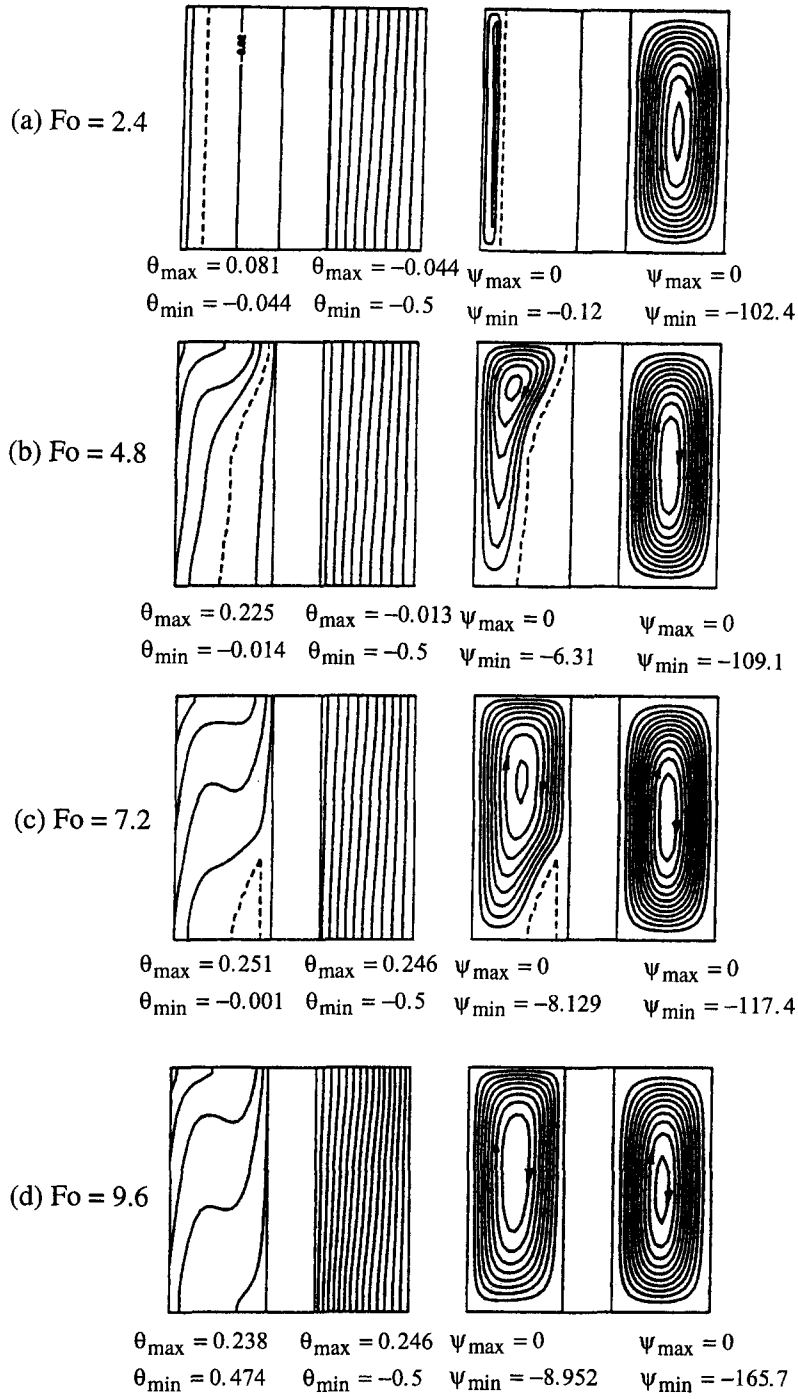

Fig. 13. Typical evolution of isotherms (left) and streamlines (right) in a PCM/air composite cell divided by a stainless steel partition of $A_d = 0.2$ with $Ste^* = 0.1$, $Sc^* = 0.5$, $Ra^* = 10^6$, and $A_p = A_a = 0.4$.

pace, as displayed in Fig. 12b, c, respectively. Further from Fig. 12c, one can observe that the highly conductive steel partition may lead to a substantially longer effective thermal protection period Fo_{cr} of the composite cell in comparison with that with the acrylic or diathermal partition. From the foregoing it may be concluded that a highly conductive partition is apparently preferable for thermal protection application of the PCM/air composite structure.

The above-described better thermal protection behavior of a PCM/air composite cell divided by a stainless steel partition can be further inferred by examining the corresponding evolution of isotherms and streamlines at four instants of the heating process

shown in Fig. 13. From the isotherm plots in Fig. 13, one can readily notice that the steel partition remains essentially isothermal, thus effectively retarding heat penetration across there. Another interesting fact observed in Fig. 13 is that after the melting front reaches the partition surface, heat is conducted effectively downward along the steel partition so as to induce melting behavior of PCM away from the steel partition. As a result, an isolated unmelted PCM block not in direct contact with the partition is detected in Fig. 13c.

CONCLUDING REMARKS

The transient conjugate heat penetration process through a PCM/air composite cell has been simulated to unveil feasibility and efficacy of using a PCM/air composite cellular structure as a thermal protection wall. By means of the mainly latent-heat absorption inside the PCM layer, heat penetration across the composite cell can be effectively delayed over a time duration of effective thermal protection, Fo_{cr}, corresponding to the instant around which the PCM melting front reaches the partition. Results from the parametric simulations for the composite cell divided by a thin diathermal partition reveal that the effective thermal protection duration of the composite cell is mainly a function of the modified Rayleigh number, the modified Stefan number, the subcooling factor, the PCM/air layer thickness ratio, and the aspect ratio of the composite cell. The increase of the modified Rayleigh number or Stefan number, resulting in the natural-convection-enhanced melting process in the PCM layer, as well as intensified natural convection flow inside the air layer, tends to degrade the thermal protection effectiveness of the composite cell; while the increase of the subcooling factor, PCM/air thickness ratio, or aspect ratio of the composite cell can greatly prolong the effective thermal protection duration. A PCM/air composite cellular structure having a shallow rectangular cell and/or a larger PCM/air thickness ratio is apparently preferred for effective thermal protection application. In addition, incorporating a highly conductive (such as stainless steel) partition of finite thickness is found to further enhance the thermal protection effectiveness of the PCM/air composite cell.

Acknowledgement—Appreciation is extended to the reviewers whose comments led to improvements of the paper.

REFERENCES

1. R. L. Bain, F. J. Stermole and J. O. Golden, Gravity-induced free convection effects in melting phenomena for thermal control, *ASME J. Spacecraft* **8,** 1000–1002 (1971).
2. W. R. Humphries and E. I. Griggs, A design handbook for phase change thermal control and energy storage devices, NASA Technical Paper 1074 (1977).
3. K. A. R. Ismail and M. R. B. Trullenque, Finned rectangular cavities filled with PCM for thermal control of electronic equipments, *Proceedings of the 6th International Symposium on Transport Phenomena in Thermal Engineering*, Seoul, Korea, pp. 237–242 (1993).
4. Y. Cao and A. Faghri, Thermal protection from intense localized moving heat fluxes using phase-change material, *Int. J. Heat Mass Transfer* **33,** 127–138 (1990).
5. C. J. Ho and C. H. Chu, The melting process of ice from a vertical wall with time-periodic temperature perturbation inside a rectangular enclosure, *Int. J. Heat Mass Transfer* **36,** 3171–3186 (1993).